APPLICATION

Design and fabrication by selective laser melting of a LIDAR reflective unit using metal matrix composite material

Boschetto Alberto[1] · Bottini Luana[1] · Macera Luciano[1]

© The Author(s) 2023

Abstract

The selective laser melting is an additive manufacturing technology able to directly fabricate full dense metal part from a virtual model. The geometrical complexity degree of freedom allows the implementation to several industrial applications such as the laser imaging detection and ranging systems. A key component of this system is the reflective unit produced with traditional technology (surface with ribs) with optimized geometry for lightweight, which must be further lightened while continuing to meet functional requirements. Aim of this work is to reach these goals by using an integrated product/process methodology which considers all the fabrication steps. A complete redesign allowed to exploit the additive manufacturing advantages of a metal matrix composite based on AA 2000 series combined with a high content of ceramic. The increased mechanical properties, such as the tensile strength of 484 MPa and Young modulus of 96GPa, combined with a lattice structure empowered the SLM capability. The component was validated via finite element method simulation focused on the most critical polishing operation. Results on static and dynamic analysis showed the 25% lightened mirror satisfies the requirements. The testing on the physical prototype confirmed the enhanced mechanical properties and the interferometric measurement proved the mirror functionality with a surface front error less than the required wavelength of 1550 nm. The work evidenced that polishing and the assembly configurations must be selected with particular care; otherwise, the final outcome is compromised for this SLMed component.

Keywords Selective laser melting · Design for additive manufacturing · Lattice structure · Metal matrix composite material · Reactive additive manufacturing

1 Introduction

The remote sensing and scanning technologies have recently received large amounts of attention by the industrial and academic communities. The term remote sensing was coined in the 1950s and lately defined as the method employing electromagnetic energy to detect, achieve, and measure the geometrical feature of a target [1].

LIDAR (laser imaging detection and ranging) is an active remote sensing technology for determining the distance to an object or surface, but it is also capable of determining the concentration of some chemical composite in the atmosphere and expanses of water [2].

✉ Bottini Luana
  luana.bottini@uniroma1.it

[1] Department of Mechanical and Aerospace Engineering, Sapienza University of Rome, Via Eudossiana 18, 00184 Rome, Italy

Active remote sensing systems emit radiation toward the target using their own energy source and detect radiation reflected from that target. An important advantage for active sensors is their ability to obtain measurements independently of sun illumination conditions and largely independent of weather conditions [3].

The source of a LIDAR system is a laser, a coherent beam of light at a precise wavelength sent toward the system to be observed, as with radar, which uses radio waves instead of laser light; the distance to the object is determined by measuring the elapsed time between the emission of the pulse and the reception of the backscattered signal [4].

The operation of LiDAR technology is based on a simple principle: knowing that the propagation speed of light is fixed, the time it takes for a light ray to travel from a source to a reflecting target, and back to the light detector (located close to the emitting light source) determines the distance traveled by the light ray and thus the distance to the target.

This measurement principle is usually referred to as time of flight (ToF). ToF can be obtained by sending through a laser a pulsed signal, and by measuring the phase and frequency of the reflected light signal with respect to a reference.

Knowing the time taken by the light ray to make the travel (reach the target and return), the distance calculation is obtained by multiplying the ToF by the speed of light and dividing by 2. In Fig. 1, a scheme of the LIDAR working principle is reported. Applying this principle at the three-dimensional level, we can obtain a cloud of points representing the distance of objects from the LiDAR sensor.

A LiDAR typically uses several components: lasers, photodetectors, and readout integrated circuits with ToF capability to measure distance by illuminating a target and analyzing reflected light [5].

Another key component for LIDAR is the moving mirror that is used to direct the laser beam onto the surface to be scanned.

There are many ways to obtain an optical scanner: oscillating plane mirrors, polygonal mirrors, and rotating mirrors. The choice of optics affects the angular resolution and the minimum and maximum distance at which the LIDAR is effective. The speed at which the image is created is determined by the speed of the mechanical scanning of the laser beam.

In the aerospace field, rotating mirrors are widely used because of their ability to scan almost 360°. This is achieved by aligning the axis of rotation of the mirror with the direction of the laser beam emitted by the source. Figure 2 shows a schematic of the rotating mirror-based system.

Many functionalities are demanded to this subsystem. Since it is under rotation, the mechanical balancing must be assured through an adequate stabilization to take care of the deformation which may affect the reflective surface. Modern LIDAR systems for aerospace applications require complex optical elements whose performance and lighter weight must be improved to meet growing application requirements. Metallic optics are a good choice to achieve the desired performance.

Mirrors manufacturing with traditional computer numerical control (CNC) technologies have limitations on mass reduction. Additive manufacturing (AM) methods offer new concepts for production of metal optics that can overcome the specific limitations of CNC technologies. Internal structures can be designed with a variety of configurations, such as periodic structures [6], honeycomb cells [7, 8], and topologically optimized structures [9–11].

The choice of metal alloy for making the mirrors depends on many factors, including the forces applied during the post-processing (e.g., polishing), the mechanical requirements, and the complexity achievable during the AM process. Various metallic alloys (invar, beryllium, and aluminum) [12] are used to make mirrors for aerospace applications, each with its own peculiarities. Aluminum is the most common choice for non-exotic or defense mirrors for its competitive structural properties. Only beryllium has an impressive specific stiffness, but it is toxic and expensive to finish since it is not directly machinable. Conversely, aluminum can be easily diamond machined [13]. Moreover, it is noticeable that optical housings are often made by aluminum, thus simplifying the assembly techniques with no

Fig. 1 Example of the working principle of LiDAR

ToF = 90 ns

Pulse sent

Laser emitter

Target

Pulse received

Detector
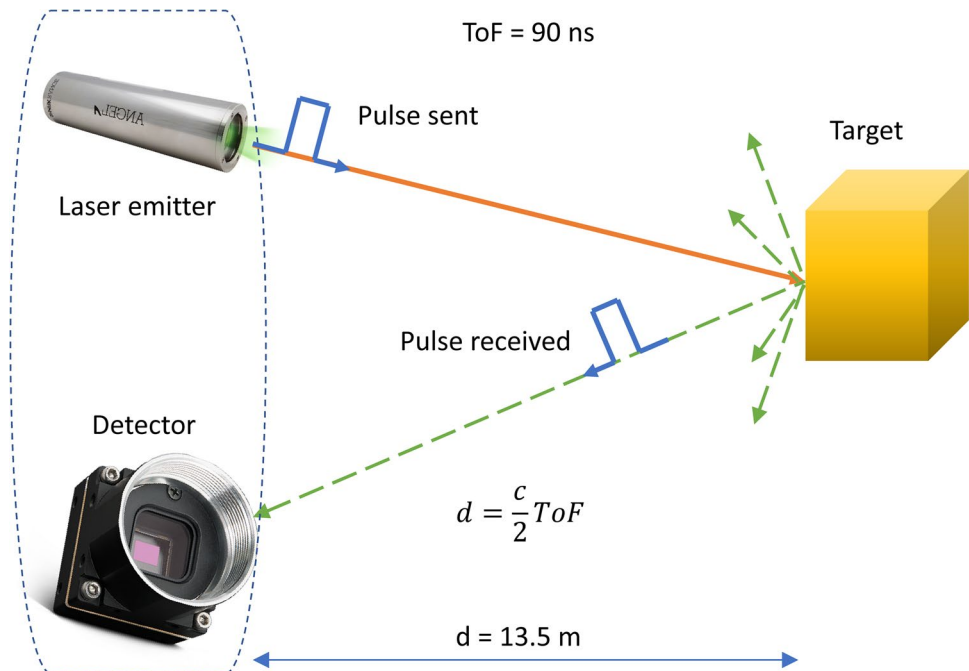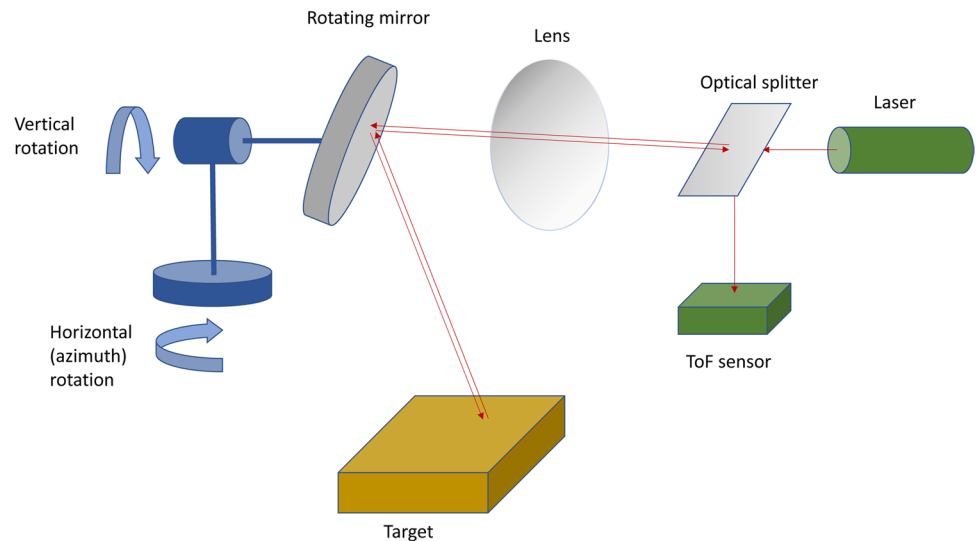
$$d = \frac{c}{2} ToF$$

d = 13.5 m

Fig. 2 Scheme of a LIDAR system

thermal coefficient mismatch [14]. In the last decades many aluminum parts were substituted by the reinforced aluminum metal matrix composites (MMC) which have become a commonplace for high-performance aerospace and automotive applications, due to their better mechanical properties for the same light mass [15]. Unfortunately, the machinability of these materials is limited by the abrasive reinforcements which negatively affect the attainable surface quality; hence, a careful selection of the cutting parameters is necessary [16]. Furthermore, for ultraprecise applications, the machining becomes challenging. In [17], an experimental research demonstrated that, by tuning accurately the cutting conditions, a surface roughness down to 20 nm can be obtained on A2024/B_4C/50p MMC fabricated via conventional method. MMC fabrications methods, such as stir casting infiltration, squeeze casting, cold spraying, diffusion bonding, and friction stir processing aim to reduce typical key issues namely the wettability, low densification, particle agglomeration, undesired chemical reactions, and microporosity [18]. Conversely, the AMed MMC is characterized by many additional laser consolidation dependent issues such as pores formation [19]. This porosity includes gas porosity and lack-of-fusion porosity. The former is due to gas entrapment and/or evaporation of certain elements during in situ exothermic reaction. The latter is associated to instabilities created by the rapid melt pool cooling which does not allow a complete gap filling.

This paper explores the possibilities given by metal AM technologies to improve the performance of the fabricated parts. In particular, it describes the re-design and fabrication of a metallic mirror using the selective laser melting (SLM) process, applicable on an industrial scale.

The motivation of the use of the AM technology is the introduction of internal lattice structures, aiming to reduce the component weight without compromising the performance. To furtherly improve the mechanical properties, an AA2024 MMC is used.

An integrated product/process methodology based on design for additive manufacturing is presented and validated via finite element method (FEM) simulation analyzing the most critical polishing operation and providing dynamic verifications. The physical final polished component was characterized by means of interferometric measurements.

2 Material and methods

2.1 Component

The 3D model of the original mirror system is shown in Fig. 3. The body, that includes the anchor shaft and the mirror plate, is made of an aluminum alloy, while the balance masses (colored in ochre in the figure) are made of tungsten. This original component is designed for CNC machining.
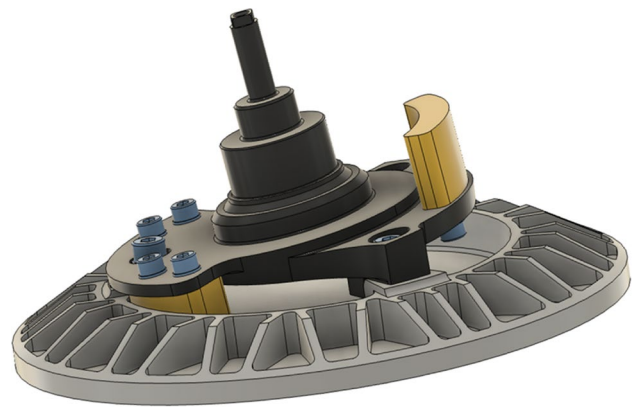
Fig. 3 Original CNC component with balance mass

To achieve the required stiffnesses on the mirror plane, the back side is stiffened through a ring with ribs on the outer perimeter. At the same time, the goal of reduced weight is accomplished by this geometry maintaining the accessibility of the tool for the back side 3D milling. In order to not propagate assembly forces to the mirror plate, the anchor points are disjoined by placing the coupling surfaces on the stiffening ring. The mirror surface is post-processed by a single point diamond turning (SPDT) and a final polishing.

The main requirements for the mirror are:

- Reduced mass
- Static balancing
- Surface front error (SFE) < 1.7 μm peak-to-valley height (P–V) at 2160 rpm rotational speed
- Constrained modal response > 1100 Hz with balancing masses
- Fabricated polished mirror SFE < λ (1550 nm) measured on five lobes (later described in Sect. 4)

The original mirror has a mass of 210 g, and it needs 205 g balancing masses.

2.2 Selected AM technology and material

The chosen AM technology is the SLM. It belongs to the category of the powder bed fusion [20]. The process uses the thermal energy provided by a laser source to selectively melts regions of a powder bed. This way it is possible to fabricate layer by layer full dense metallic components characterized by very complex geometries and good mechanical properties [21, 22].

To satisfy the component requirements reported in Sect. 2.1 and improve its performance, the implementation of a new alloy available only for the SLM process, the AA2024 RAM10 produced and patented by Elementum 3D, is proposed. The powder feedstocks were produced by gas atomized reaction synthesis of inoculant/reinforcement particulates within the AA2024 matrix. The input material mixture is composed by weight 75.19% aluminum/4.5% magnesium alloy powder, 18.23% titanium/6% aluminum/0.4% vanadium powder, and 6.58% boron carbide powder. The outcome is composed by aluminum/4.5% magnesium matrix by volume 85% and ceramic reinforcing phases by volume 15% of titanium and vanadium diborides and carbides [23]. Due to the proprietary powder design, the exact composition and the nature of the resulting products cannot be reported. Particular care must be paid to the feedstock powder and, in particular, to the particle diameters of the reactive constituent since a size in a specific range can enhance the reactivity [24] and play an important rule for the uniform refinement [25]. In Fig. 4a, a SEM image of the powder feedstock is shown. The ceramic particles, which are lighter in the image, are small and have a spherical shape. The aluminum powder exhibits some oblong shape, as expected for this atomized material. By using a digital image processing procedure designed for the purpose in Wolfram Mathematica 13.01, the small lighter particles were separated and segmented. The aluminum particles were found by subtraction, and an interpolation was provided for lacking zones. A morphological component was applied to find regions. In Fig. 4b, the cyan and yellow circles represent the detected aluminum and ceramic particles, respectively. At nanoscale, the attractive Van der Waals forces facilitate the agglomeration which can lead to a microstructural inhomogeneity and reduce the strengthening effect of the reinforcement [26]. Nevertheless, in the Fig. 4a and b, only some occasional agglomerates can be observed. The size distributions were analyzed and graphed for the two distinct components. The aluminum powder is characterized by the particle volume distribution shown in Fig. 4c. The average particle size is 36 μm; the D10 and D90 are 21 μm and 56 μm, respectively. This distribution is in line with typical distribution used for SLM processing. Conversely, the distribution of the ceramic is bimodal, as can be observed from the Fig. 4d. A sub-micron particles range between 200 and 800 nm while larger particles are approximately between 5 and 20 μm. This is in agreement with the manufacturer's document [27].

Its mechanical properties are showed in Table 1. Among them, the most important for this specific component is the extremely high stiffness of 100 GPa (with respect to the usual 70 GPa of the most aluminum alloys) at detrimental of slightly increased density.

This alloy is a MMC material directly generated by the SLM process itself [29]. The method belongs to the so-called reactive additive manufacturing (RAM) technology which allows synthesis of advanced materials during the AM process, as illustrated in Fig. 5. The concept behind RAM is a chemical reaction triggered by laser, where precursor components react together to form the final product. Therefore, the chemical composition of the precursors is different from the composition of the ceramic elements in the matrix of the produced MMC aluminum alloy.

This peculiarity allows the use of precursor materials with a preferred size and shape for a good powder flow. RAM technology utilizes exothermic chemical reactions to synthesize product materials during the additive process to improve printability and properties. The RAM process enables formation of advanced MMCs that combine a metal matrix and high strength reinforcing ceramic or intermetallic phases [23].

In the AA2024 RAM10, the elements are basically the alloy Al 2024 (particle size D50 of 36 μm) and precursor of ceramic particles (D50 of 20 μm). When exposed to the laser energy, the reaction starts forming sub-micron
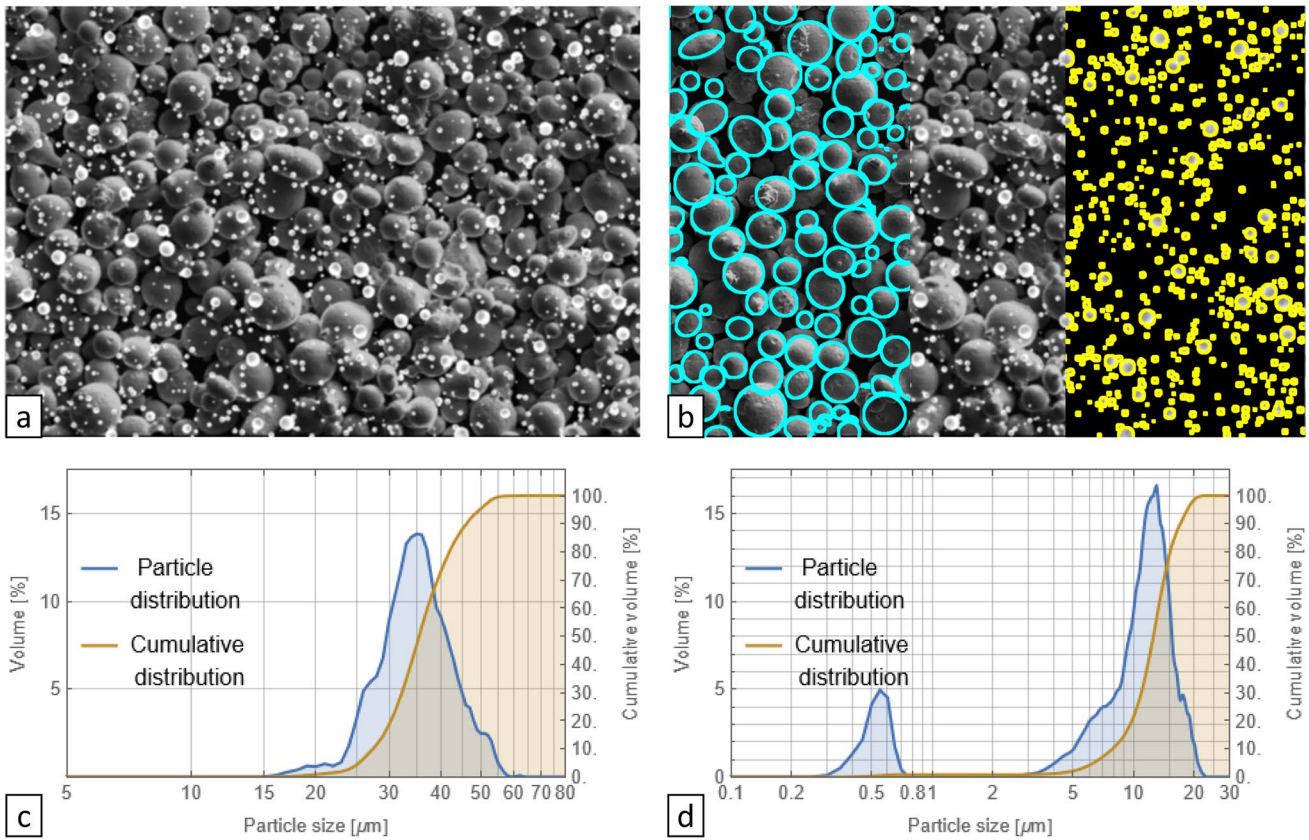
Fig. 4 Powder feedstock SEM image (**a**), detected aluminum and ceramic particles (**b**), particle size distribution of the aluminum powder (**c**), and the reinforcing ceramic (**d**)

Table 1 AM Aluminum alloy RAM10-2024 mechanical properties [28]

	AA2024-RAM10		
	As built	T6 treated	After stress relieve
Ultimate tensile strength	465 MPa	555 MPa	484 MPa
Yield strength	379 MPa	535 MPa	377 MPa
Young modulus	96GPa	100 GPa	~96GPa
Elongation at break	~2%	~2%	~2.9%
Density	2.95 g/cm^3		

sized precipitates (of about 0.2 μm) through in situ synthesis from the larger precursors. The nano-precipitates act as highly stable reinforcement phase producing highly favorable microstructures and enhancing material performance. Moreover, precursor materials can have lower melting temperatures than the final product to facilitate the laser fusion and assist in achieving full density. The nano-precipitates act as nucleants during solidifications producing an equiaxed final microstructure. A tailorable
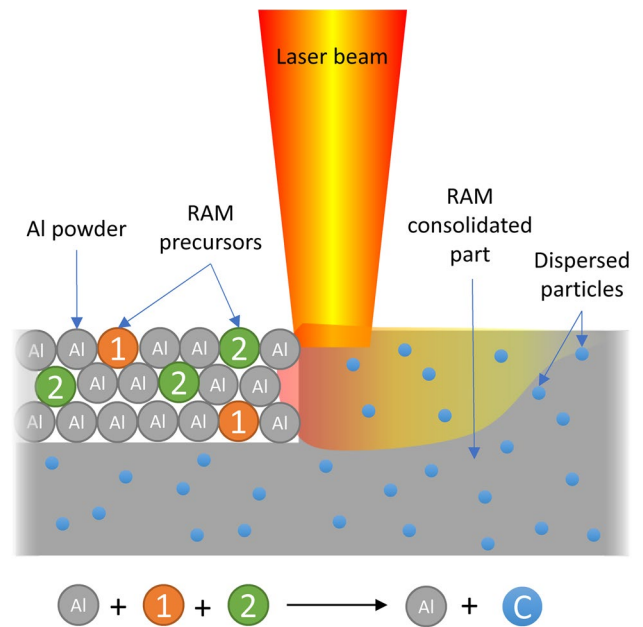

Fig. 5 RAM concept

increasing of strength, stiffness, and modulus can be obtained by increasing the percentage of ceramic. It is well-known that 2024 aluminum alloy printability is plagued by the hot tearing, resulting in a reduced performance with respect to the wrought counterparts. It is commonly observed that this susceptibility is closely related to the formation of columnar grains which grew epitaxially across layers and spanning between layers [30, 31]. Typically, the SLMed 2024 alloy is characterized by a high fraction of cracks propagating along the building direction as well as the horizontal plane. A crack network is commonly formed as shown in Fig. 6a. The columnar structure and the hot-tearing cracks provide easy path for the crack propagation during the tensile test, resulting in a material embrittlement and anisotropic mechanical properties which are below sufficiency for industrial application [32]. Furthermore, some alloying elements have high vapor pressures and can evaporate during laser processing. The vapor plumes, spattering, porosity, and again cracks are possible issues. For this reason, the SLM aluminum alloy selection is mainly oriented to other series such as the 4000, 6000, and 7000 [33]. With RAM, a small fraction of synthesized ceramic allows eliminating the printability issues as shown in Fig. 6b: an even dispersion of ceramic is observed, and cracks are avoided.

The case of Al 2024 RAM10 is particularly interesting as its reaction adds energy to the process being it exothermic, contributing to increase build speed. When compared to the most used AlSi10Mg, the increasing in productivity is remarkable. Tests carried on EOS M290 showed that the average deposition rate of EOS AlSi10Mg is 5.1 mm^3/s whilst the AA2024 RAM10 provides 7.12 mm^3/s accounting for an increasing of 39% [27].

2.3 Fabrication

For the fabrication, an EOS M290 was used. This machine is equipped with a 400 W ytterbium fiber continuum laser characterized by a beam spot diameter of 100 μm and a building volume of $250 \times 250 \times 325$ mm^3. The process was carried out in an argon inert atmosphere with less than 0.1% oxygen, and the building platform was preheated at 200 °C to reduce residual stresses.

The employed process parameters were specifically optimized for the use of AA2024 RAM10 alloy powders and reported in Table 2.

A specific optimization of the parameters was performed to minimize the roughness on the surface of the lattice, as the typical roughness on 45° walls can significantly affect the robustness of the lattice structure described in the following. It is well-known that a small nominal size for the structure can be affected by the coarse microgeometry of the SLMed surfaces resulting in a reduced real resistant section [34]. In this work, the aim is the weight reduction thus thin lattice struts are implemented. For the purpose, the total roughness Rt must be necessarily reduced. Typical values for an AlSi10Mg processed by SLM exceed 140 μm [35], e.g., in the unlucky event the valleys are at the opposite side of a strut 0.8 mm in diameter, the 58% reduction in resistant section occurs. The selected material and exposure parameters allow achieving a Ra less than 6 μm on 45° slope. The corresponding measured Rt is only 50 μm leading to a loss in the resistant section less than 23% which is acceptable for this application.

The preprocessing for SLM fabrication was provided in Materialise Magics. A vertical building was selected to reduce interaction issues between the powder, the part, and

Fig. 6 SLMed AA2024 micrograph showing cracking (**a**); SLMed AA2024-RAM10 with a uniform dispersion of ceramic and without cracks (**b**)
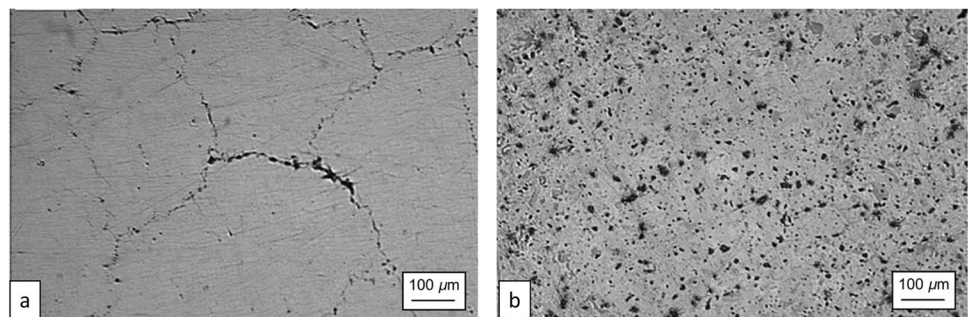

Table 2 AA2024 RAM10 process parameters

Stripes		Upskin		Downskin	
Hatch distance	0.19 mm	Hatch distance	0.19 mm	Hatch distance	0.18 mm
Laser speed	1250 mm/s	Laser speed	1000 mm/s	Laser speed	2000 mm/s
Laser power	370 W	Laser power	370 W	Laser power	370 W
Beam offset	0.02 mm	Layer thickness	0.09 mm	Layer thickness	0.09 mm

the recoater. This way, the support structures were designed reducing efforts at the post-production phase (CNC milling of mirror surface and coupling interface). The model and support structures files were loaded in EOSPRINT 2.4 software to assign the exposure parameters and check the laser path before building phase.

After the fabrication, the detachment from the building platform was carried out through a bandsaw. Wire electrical discharge machining (EDM) was not selected to avoid water contact with the aluminum powder trapped inside the trabecular structures. If a powder-water moisture occurs, a fast oxidation reaction takes place and powders can lock inside.

The inner powders removal was carefully controlled and a T6 thermal cycle was provided in a Nabertherm LH120/14 controlled atmosphere hoven. The heat inducing laser fusion process results in a significant residual stress and, therefore, in an unstable mirror [36, 37]. A stress relieving heat treatment was applied according to the following characteristics: the mirror was slowly heated at 5 °C/min rate up to the soaking temperature of 550 °C and maintained for 1.5 h; after a water quenching, an aging at 165 °C for 24 h was provided.

A tensile test was carried out to validate the use of this material for the specific component. A 50 kN Zuick Z050TN universal testing machine was employed under quasi-static loading conditions, imposing a ramped displacement at 0.05 mm/min speed. The samples geometry was a dogbone, with a square cross-section of 5.72×4.00 mm^2 and a nominal gauge length of 25.40 mm in accordance with the standard ASTM E8/E8M [38]. The specimen was printed in the same building platform of the mirror.

Aluminum MMCs fabricated via conventional processes are generally directly machinable. Conversely, SLMed MMCs show internal defects that arise during the surface finishing. Some elements in the aluminum alloy (Mg, Zn) have high vapor pressure and can easily evaporate during laser melting [33]. This can result in vapor plumes, spatter, reduced printability, cracking, and porosity. This last issue is particularly pronounced since the reinforcement particle lack-of-fusion, key hole formation, and gas entrapment [39, 40]. The pore dimension is up to 100 μm. This issue is really critical if a particular smooth finishing is requested. A preliminary experimentation confirmed the SLM part porosity and avoided the possibility to directly machine the SLMed surface. In [41], the direct polishing of SLMed AlSi10Mg mirror highlighted an unacceptable roughness. Conversely, the application of a SPDT allowed to assure a very good result. In the same work, the application of nickel plating resulted in similar roughness as well. For this reason, in this work, the plate was subjected to a very fine SPDT and a subsequent nickel plating. This coating was selected to have a good thermal expansion compatibility which deeply reduces the deformation over temperature of high performance mirrors in environmental extreme conditions. The SPDT was

performed by Edmund Optics Ltd Nether Poppleton, York, UK, by using a Moore Nanotech Multi-Axis UPL Diamond Turning Machine. The coating was performed by an electroless nickel plating with a few percent of phosphorus. A subsequent baking at 200 °C for 8 h was applied to increase the mirror hardness [42].

The polishing operation is the most critical one since the internal structures affect the mirror surface and deteriorate the accuracy [12]. This phenomenon is called print-trough effect or quilting originally studied in [43] and well-known in the vacuum chuck mounting of mirrors [44]. Hence, particular care was addressed to this aspect in the mirror design. The Autodesk Nastran 2016 was employed to undertake static simulation and predict local deformation caused by this last stage.

The final optical surface was characterized by a Zygo® VeriFire™ High Resolution Interferometer. Surface maps as well as P–V measurements were achieved.

3 Results and discussion

3.1 Re-design of the component

The main objective of the re-design is the weight reduction maintaining the strict mechanical constraints on deformation and static balance as the part rotates at high speed. For the scope, the mirror body and inner lattice structures are modeled using FEM.

The choice was made to use a star trabecular structure which allows excellent quality in the fabrication of the beams, when properly inclined, using SLM technology.

Using the simulation, it is possible to choose the best lattice structure that would provide the maximum lightening of the mirror. Obviously, the greater the length of the beams in the lattice structure, the greater the volume of the cell and thus the greater the weight reduction.

The so-called design space is shown in Fig. 7a. A small modification of this space was provided to avoid overhanging surfaces. A minimum thickness of 0.8 mm was imposed on the back skin to ensure their manufacturability with SLM technology, and the same limit was imposed on the thickness of the beams [45, 46]. The front skin was fixed to 2 mm. The resulting empty space to fill by the lattice structures is reported in Fig. 7b. It is variable and two zones can be found, namely the A and B in the figure. The former has a constant thickness of 7 mm overall the internal mirror center. The latter is related to the external ring with a variable thickness up to 12.5 mm.

Since the simulation on the entire geometry is computationally intensive, a prescreening was undertaken on a reduced geometry characterized by the 25 mm sided ashlar shown in Fig. 8a. To consider a variable thickness of the

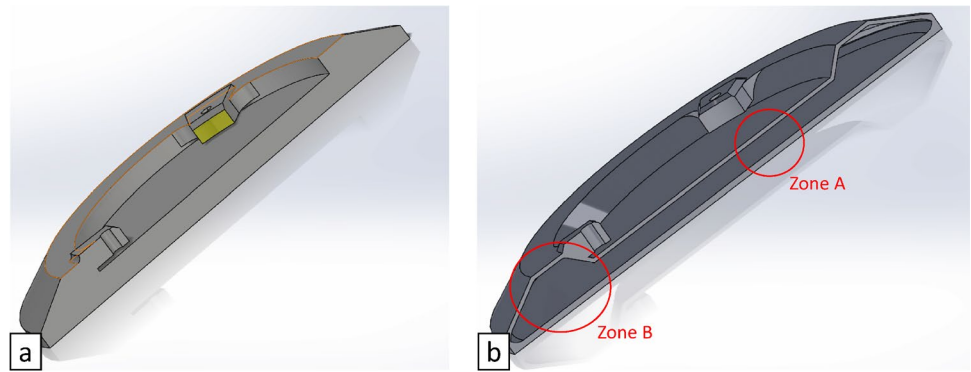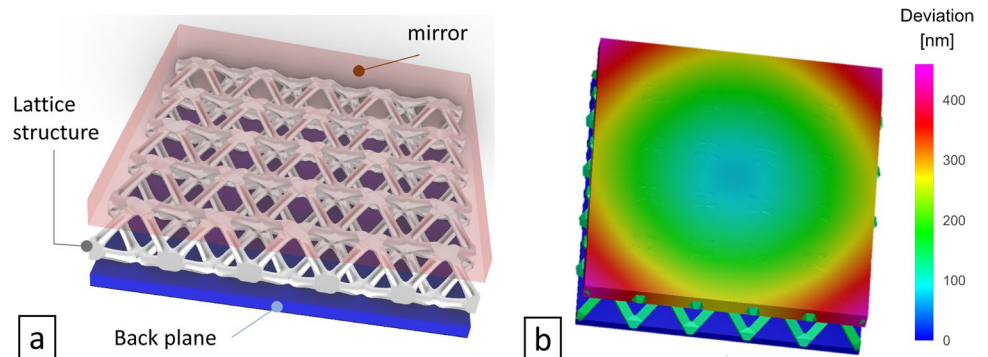**Fig. 7** Design space (**a**) and skinned modified mirror (**b**)

Fig. 8 Transparent view of the reduced geometry with 1 mm backplane, 0.8 mm beam thickness transparent view of the 5×5x5 mm.^{3} cell (**a**), and result of the simulation (**b**)

design space, 7 mm and 12.5 mm cell sizes were considered in the simulation. The periodic lattice structure needs to be trimmed off this zone, and the resulting mechanical resistance can be affected by the sample thickness.

Notwithstanding this approach does not take into consideration the whole geometry and the aspects related to the mirror assembly, it can give comparative analysis between different combinations of the abovementioned parameters. The simulation was undertaken considering the most critical polishing operation. A maximum pressure of 0.02 MPa was frontally applied to the mirror to simulate this effect [47]. In Fig. 8b, the result of the simulation in the case of 1 mm back skin thickness and 0.8 mm beam size is reported. As expected, a symmetrical deflection is observed, and a 456 nm maximum deviation was found at the corners since they are not constrained by lateral elements.

The simulation was repeated in a factorial plan by changing the values of the lattice cell size, the beam thickness, the back skin thickness for the two testing sample volumes according to the Table 3.

The volumes of the sample and the volume ratio, i.e., the actual to the occupied volume ratio, were calculated accordingly. Figure 9a shows the outcomes for 25 × 25 × 7 mm^3 testing sample volume. As expected, the cell size of 5 × 5 × 5 mm^3 (cases 1–4) allows to obtain smaller displacement than the 7 × 7 × 7 mm^3 (cases 5–8) at detriment of the volume ratio. It is evident that the back skin

thickness effect (e.g., cases 1 and 2) on the maximum displacement is greater than the beam thickness effect (e.g., cases 1 and 3). Bigger displacements and smaller volume ratios are observed for 25 × 25 × 12.5 mm^3 with similar behavior (Fig. 9b). Most of the cases shows opposite outcomes. A good compromise is the 7 × 7 × 7 mm^3 cell with 1 mm beam size and 1 mm back skin thickness. This case allows gaining a good weight reduction and an intermediate maximum displacement. Furthermore, this configuration presents important benefits by means of the following elements not included in the previous analysis:

- The easiness of removing powder trapped inside the part at the end of the printing process;
- Thicker beams allow better printability because they tend to vibrate less in contact with the recoater blade.

The lattice structure was filled within the design space and the full object was simulated for the polishing operation. The part was fixtured by using 3 holes (Fig. 10a) later employed for the assembly of the mirror. Results of this configuration (case A) are summarized in Table 4. As expected, the maximum displacement was much bigger than the previous value simulated in the preliminary screening (Fig. 10b). However, the mirror front surface appears quite uniform: the SFE is 2356 nm. The total weight of the mirror is 157.79 g. This is a marked decreasing as compared with the initial 210.0 g.

Table 3 Results of the prescreening simulation tests on the reduced geometry

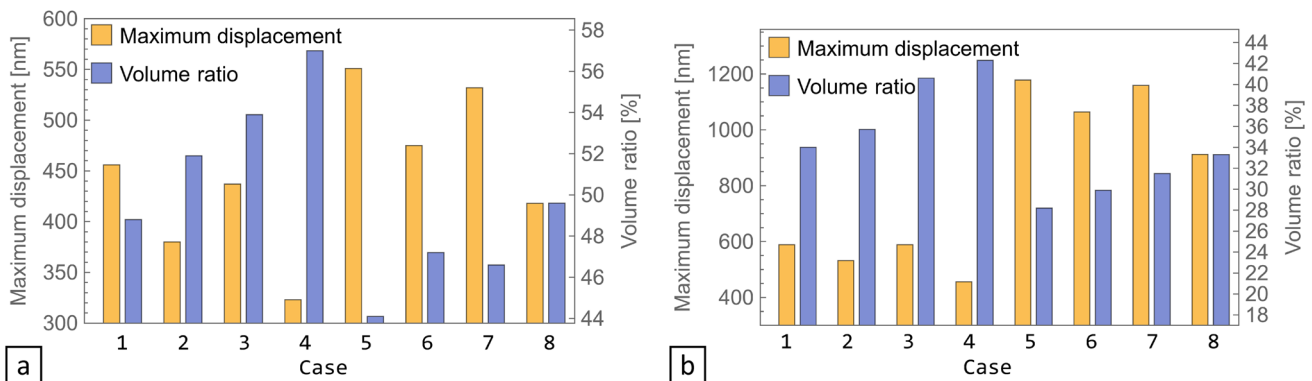| Testing sample volume [mm^3]	Case	Lattice cell [mm^3]	Beam thickness [mm]	Back skin thickness [mm]	Mirror skin [mm]	Maximum displacement [nm]	Sample volume [mm^3]	Volume ratio []
25×25×7	1	5×5×5	0.8	0.8	2	456	2135	48.8%
	2	5×5×5	0.8	1	2	380	2270	51.9%
	3	5×5×5	1	0.8	2	437	2358	53.9%
	4	5×5×5	1	1	2	323	2493	57.0%
	5	7×7×7	0.8	0.8	2	551	1930	44.1%
	6	7×7×7	0.8	1	2	475	2065	47.2%
	7	7×7×7	1	0.8	2	532	2037	46.6%
	8	7×7×7	1	1	2	418	2172	49.6%
25×25×12.5	1	5×5×5	0.8	0.8	2	589	2656	34.0%
	2	5×5×5	0.8	1	2	532	2791	35.7%
	3	5×5×5	1	0.8	2	589	3172	40.6%
	4	5×5×5	1	1	2	456	3307	42.3%
	5	7×7×7	0.8	0.8	2	1178	2203	28.2%
	6	7×7×7	0.8	1	2	1064	2338	29.9%
	7	7×7×7	1	0.8	2	1159	2464	31.5%
	8	7×7×7	1	1	2	912	2599	33.3%

Fig. 9 Results for maximum displacement and volume ratio for 25×25×7 mm^3 (**a**) and 25×25×12.5 mm^3 (**b**) testing sample volume

Other simulations were carried out to understand if the back skin can be reduced. The mirror without the back skin (case B) is shown in Fig. 10c. This case is critical since it is well-known how the back skin helps to reduce the bending of the mirror [13]. This is confirmed by the simulation reported in Fig. 10d: the maximum displacement is 61,560 nm, very close to the SFE. It is evident the surface is subjected to an almost pure bending deformation confirming the rule the skin has in this application. The case C considers a back skin only on the central disk as shown in Fig. 10e. The total deformation is markedly reduced to only 8702 nm making this solution interesting since its weight is only 128.01 g. Unfortunately, the absence of the back skin in the external disk allows for bending distortion in this zone, and

the mirror front surface is characterized by a SFE 6878 nm greater than the case A (Fig. 10f).

The last configuration (case D) considers a totally different way to fixture the part: the 3 holes are substituted by a back plane. As in the case A, a full back skin is adopted (Fig. 10g). The results claim that the central part of the mirror is almost undeformed, and a slight bending takes place on the external ring. The maximum displacement is very small and almost located onto the front mirror surface leading to an SFE of 1140 nm (Fig. 10h). However, this solution is technically difficult to provide in a real polishing operation; more important, it does not reflect the final assembly configuration where the forces exerted by the screws will affect the final deformed shape in a way different from the
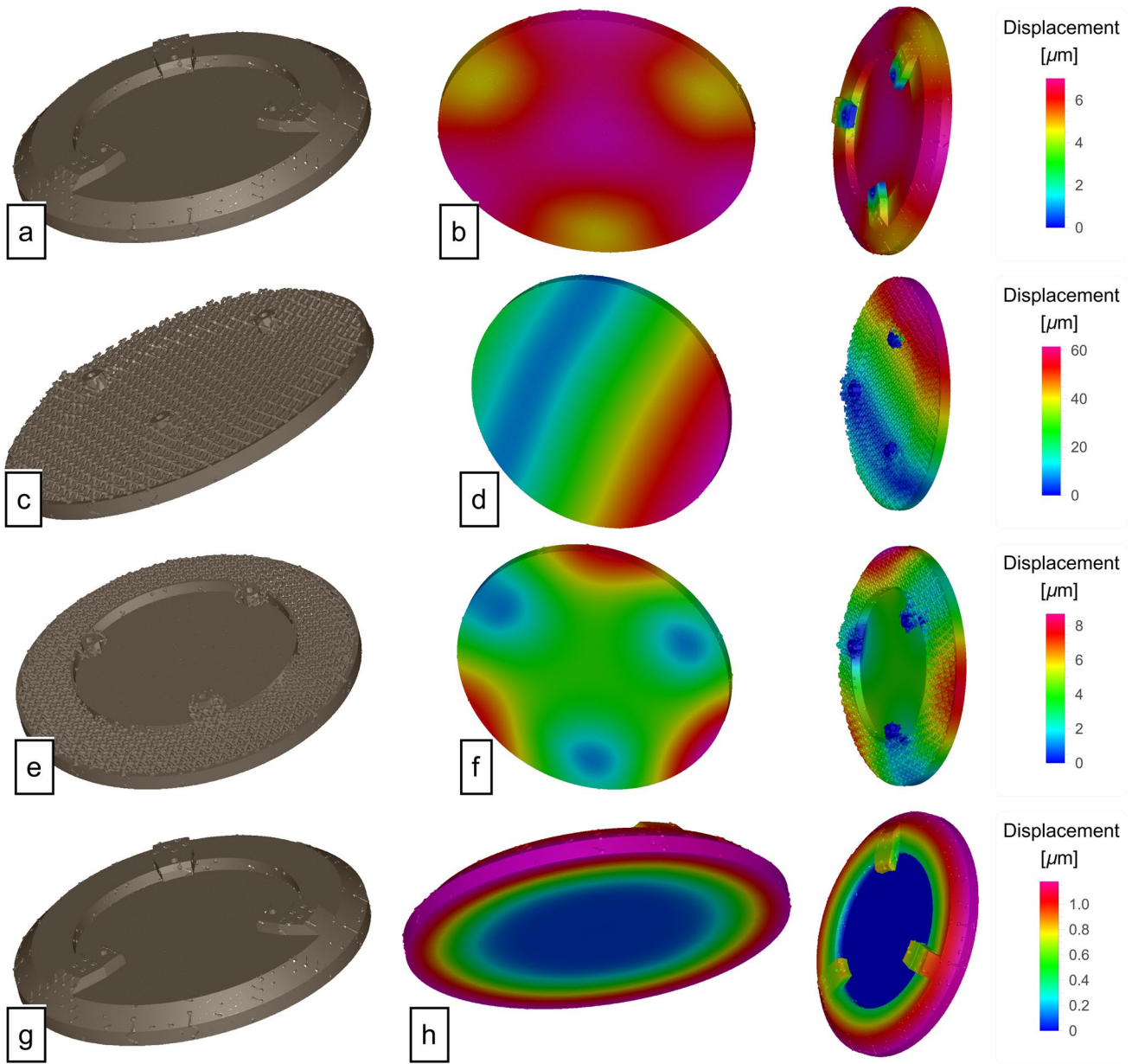
Fig. 10 Simulation results for the investigated cases

Table 4 Simulated maximum displacement, SFE, mirror weight for the investigated cases

Case	Fixturing constrains	Back skin	Maximum displacement [nm]	SFE [nm]	Weight [g]
A	3 holes	Full	7030	2356	157.79
B	3 holes	None	61560	58710	117.39
C	3 holes	Partial	8702	6878	128.01
D	Back plane	Full	1178	1140	157.79

simulated one. Therefore, the mirror was fixtured by using the three holes for the polishing operation (case A).

A static balancing of this lightened mirror was provided. In particular, the original mass of 205 g was reduced to 154 g. Therefore, the mirror total mass was cut by 25% (from 415 to 311.8 g).

The selected structure was verified by means of the FEM analysis. The simulation under the rotational speed is shown in Fig. 11a. Most of the centrifugal force effects are located on the shaft assembly system while the mirror surface returned a SFE of only 675 nm which is in line with the requirement of 1700 nm. The shape of the deformation is close to a bending. Another simulation was undertaken adding the forces exerted by the tightening of the screws (Fig. 11b). The results highlighted a bigger deformation on the mirror: in this case, the SFE is 1680 nm, very close to the limit of the requirement. This outcome underlines that the assembly of a mirror lightened by lattice structures is a critical operation which may compromise the component functionality.

The last verification regards the evaluation of the frequencies of the rigid modes in free and constrained configurations. In the former, the shapes of the first three main modes along with the three axes are shown in Fig. 12a–c. All the frequencies comply with the minimum design requirements (> 4000 Hz). In the latter, the constrained configuration shows lower frequencies as expected (Fig. 12d–f). The lower required limit of 1100 Hz is satisfied also in this case.

Fig. 11 Simulation of the assembled mirror under rotation (**a**) and tightened by the screws (**b**)
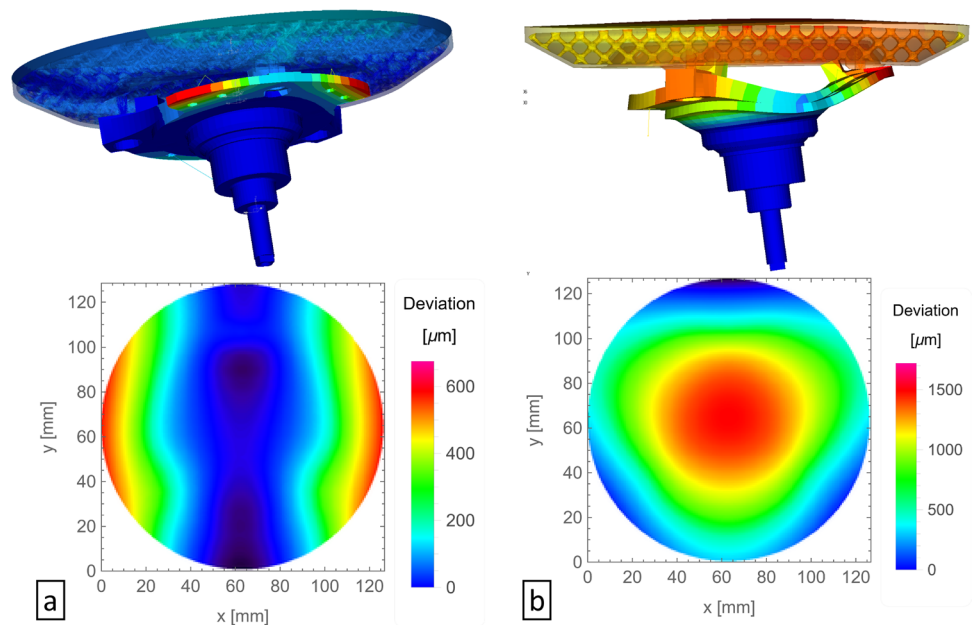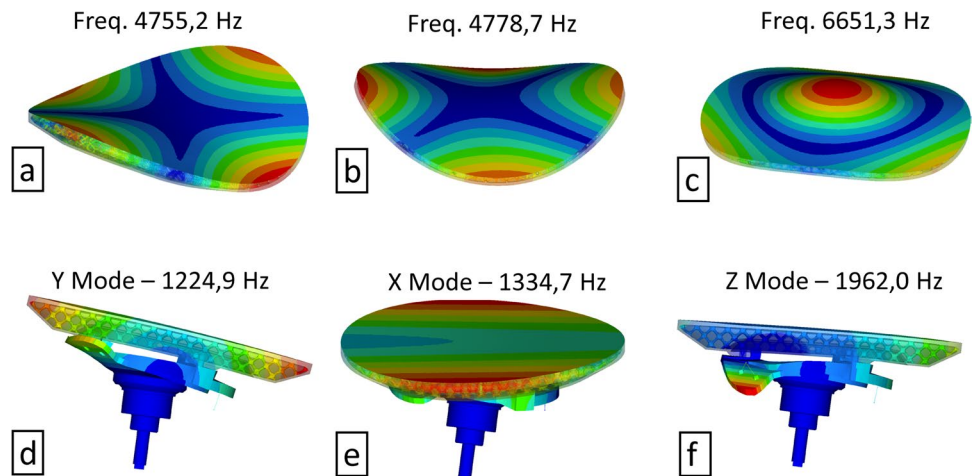

Fig. 12 Modal simulations in the free configuration along axes x (**a**), y (**b**), and parallel to the shaft axes (**c**); modal results in the constrained configuration along the x axes (**d**), y axes (**e**), and parallel to the shaft axes (**f**)

3.2 Mirror fabrication and testing

The configuration passed all the required simulative test and thus it was fabricated trough SLM. Figure 13a shows the mirror before its detachment from the building platform. In Fig. 13b, the support structures were removed. The holes deputed to remove the powder trapped in the lattice empty spaces are visible. Figure 13c reports a mirror sectioned to show internal features. After the secondary finishing processes (SPDT, nickel plating and polishing), the mirror shows a very shiny surface without naked eye visible defects (Fig. 13d).

The tensile tests are reported in Fig. 14. As shown, the three specimens trends highlight a very good repeatability.

Fig. 13 SLMed mirror after the fabrication (**a**), after the platform detachment and powder removal (**b**), sectioned mirror (**c**), finished and mounted mirror (**d**)
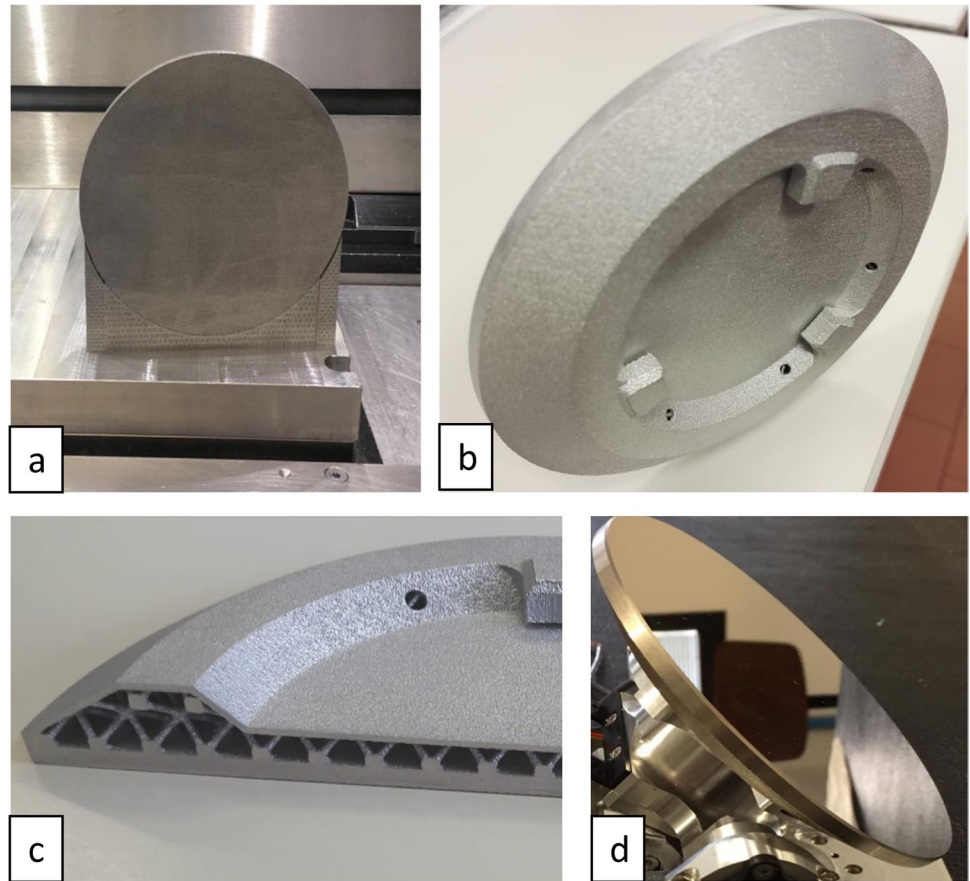
Fig. 14 Tensile tests curves

Young modulus: 95.6±0.8 MPa
Yield strenght: 495.3±7.4 MPa
Ultimate strenght: 523.5±13.3 MPa

Specimen 1
Specimen 2
Specimen 3
0.2% yield
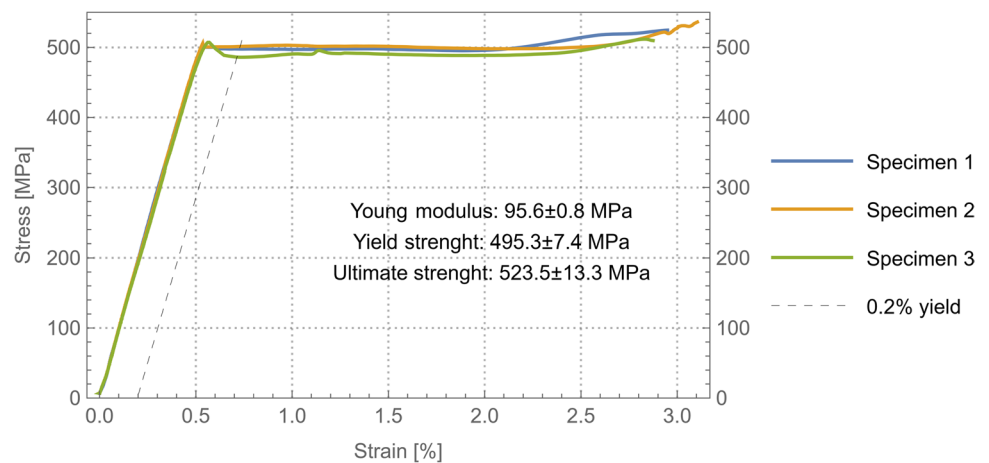
The ultimate tensile and yield strengths give values according to the expected results. The curves are characterized by a little peak after the elastic behavior and a flat deformation at the constant yield strength stress value. After 2% deformation, the stress increases, and at about 3%, the break occurs, as expected. The Young modulus calculated on the curves is close to the desired value of 96 GPa.

The mirror was verified by means of the interferometric measurement. Two testing configurations were considered: free and screwed. In the former the mirror was simply placed on the support. In the latter, the mirror was fixtured by tightening the screws used for the final assembly with the nominal torque of 1.6 Nm required by the application.

Figure 15a shows the 3D map of the displacements for free configuration. On the bottom right, the intensity plot is reported. The dashed line indicates that all the mirror surface (123.5 mm in diameter) is considered in this evaluation. About 3442 nm SFE is detected for this case. The root mean square is 522 nm. The free configuration does not correspond to the polishing conditions. In fact, a totally different interferometric result is obtained when the mirror is fixtured through the screws as shown in Fig. 15b.

Although the SFE is quite the same (3457 nm), a better uniformity is observed. This is expected since the screws apply forces distorting the geometry during the polishing which are released when the mirror is disassembled. As required from the specification, the SFE must be calculated in 5 circle lobes having one half of the diameter of the mirror. The central lobe in the free configuration is shown in Fig. 15c. This zone is characterized by circular artifacts. Probably, these scratches are the results of vibrations induced during the SPDT operation. These artifacts were not deleted by the polishing and have a P–V height of about 60 nm and the SFE is 353 nm. In the screwed configuration, the scratches are obviously present, but they are less visible since the SFE is 1201 nm (Fig. 15d). In the other lobes, the screwed configuration shows worst results: in the top (Fig. 15e) and left (Fig. 15g) zones, the free configuration exhibits 1937 nm and 1687 nm, respectively. These values do not comply with the specification. In the screwed configuration, the top zone is markedly more homogeneous, as shown in Fig. 15f. Notwithstanding the zone is far from the screws, the deformation is markedly reduced (SFE 729 nm). Conversely, the left lobe shown in

Fig. 15 Interferometric measurement of the mirror surface in the free (**a**, **c**, **e**, **h**) and screwed (**b**, **d**, **f**, **h**) configuration. Whole analyzed area (**a**, **b**) and some lobes (**c**–**h**)
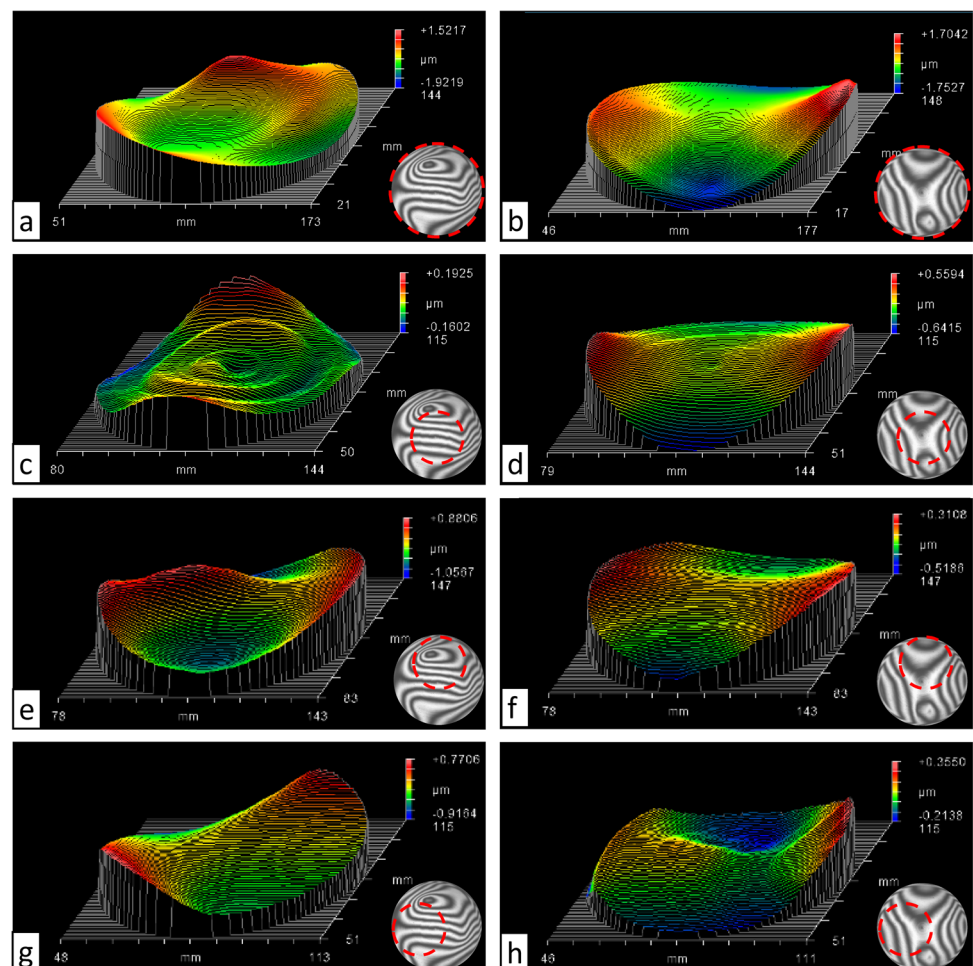
Fig. 16 SFEs of the surface lobes for free (**a**) and screwed (**b**) configuration
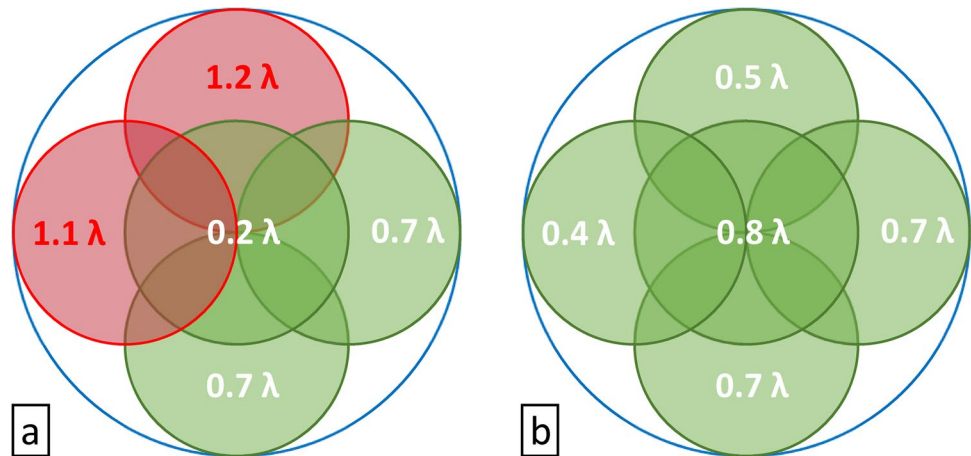

Fig. 15h is close to a screw and a bump can be observed; the SFE is 569 nm.

The analysis undertaken on all the lobes is summarized in Fig. 16a and b for the free and screwed configuration, respectively. The displacements are expressed as multiples of λ. In the free configuration, the top and left lobes are out of the specification limit, as evidenced in red. The other lobes are within the requested values. In the screwed configuration, all the measurements carried out on the single lobe complies with the specification. This result demonstrates that the final front mirror displacements can exceed the tolerances if the polishing operation is not performed in the same configuration the mirror is assembled.

4 Conclusion

This work presents an integrated redesign for LIDAR mirror fabrication employing SLM and MMC materials as enabling technologies in order to reduce the mass of spinning parts. Innovative and challenging aspect of this work are related to the employment of SLM for producing complex lattice structure MMC blank for subsequent SPDT, Ni-plating, and polishing operations. The method considers all the fabrication steps and provides a selection for lattice structures as well as the mirror configuration. Simulations and physical testing provided the following conclusions:

- The prescreening simulation allowed the selection of a lattice structure with good compromise between mass reduction and maximum displacement;
- A fully back skinned mirror is the best solution since the back skin absence or the partial reduction determines an unacceptable worsening of the SFE;
- The direct machining of the SLMed MMC part is compromised by the known laser processing issues;

- The selected configuration allowed a 25% total mass reduction of static balanced mirror (from 415 to 311.8 g), compared with traditional technology (surface with ribs) mirror with geometry optimized for lightness;
- The dynamic analysis showed smaller displacements than the case the mirror is assembled via tightening the screws;
- The modal analysis demonstrated the compliance with the requirements of a constrained modal response greater than 1100 Hz;
- The tensile test confirmed the expected mechanical properties of the SLMed MMC, namely a ultimate strength of more than 500 MPa and a Young Modulus of 96 GPa;
- The interferometric measurement pointed out that the fabricated mirror must be finished and measured in the same way as the final assembled configuration; otherwise, it exceeds the required limits, as evidenced in the free arrangement.

The work underlines that the AM metal mirror fabrication can have an important progress by combining the geometrical design with new high performance MMC materials. However, the integration with the secondary finishing operation and the deformation induced by the assembly are of primary importance to assure the functionality.

Further development could involve integrating the balancing mass (with associated shift of the center of mass) and the shaft to achieve further weight reduction.

Data availability Not applicable.

References

1. Sabins FF (2020) Remote sensing principles and interpretation, 4th edn. Freeman, New York
2. Kovalev VA, Eichinger WE (2004) Elastic Lidar: theory, practice, and analysis methods. Wiley-Interscience
3. Dong P, Chen Q (2017) LiDAR remote sensing and applications. CRC Press. https://doi.org/10.4324/9781351233354
4. McManamon P (2019) LiDAR technologies and systems. SPIE Bellingham, Washington. https://doi.org/10.1117/3.2518254
5. Hey JV (2014) Design, implementation, and characterization of a novel lidar ceilometer. Springer Cham, London. https://doi.org/10.1007/978-3-319-12613-5
6. Diegel O, Nordin A, Motte D (2019) A practical guide to design for additive manufacturing. Springer Singapore. https://doi.org/10.1007/978-981-13-8281-9
7. Milan B (2016) Laser additive manufacturing. Materials, Design, Technologies, and Applications. Woodhead Publishing, Cambridge
8. Hilpert E, Hartung J, Risse S, Eberhardt R, Tünnermann A (2018) Precision manufacturing of a lightweight mirror body made by selective laser melting. Precis Eng 53:310–317. https://doi.org/10.1016/j.precisioneng.2018.04.013
9. Fan Y, Dong D, Li C et al (2021) Research and experimental verification on topology-optimization design method of space mirror based on additive-manufacturing technology. MDPI Machines 9(12):354. https://doi.org/10.3390/machines9120354
10. Liu G, Guo L, Wang X, Wu Q (2018) Topology and parametric optimization based lightweight design of a space reflective mirror. Opt Eng 57(7):1. https://doi.org/10.1117/1.OE.57.7.075101
11. Sahu R, Patel V, Singh S, Munjal B (2017) Structural optimization of a space mirror to selectively constrain optical aberrations. Struct Multidiscip Optim 55(6):2353–2363. https://doi.org/10.1007/s00158-016-1616-x
12. Zhang K, Qu H, Guan H et al (2021) Design and fabrication technology of metal mirrors based on additive manufacturing: a review. Appl Sci 11(22):10630. https://doi.org/10.3390/app112210630
13. Woodard K, Myrick B (2017) Progress on high-performance rapid prototype aluminum mirrors. Adv Opt Def Appl UV through LWIR II 10181:101810T. https://doi.org/10.1117/12.2263319
14. Heidler N Hilpert E, Hartung J, Albert T (2017) Lightweight structures for metal mirrors. EUSPEN Dimensional Accuracy and Surface Finish in Additive Manufacturing, KU Leuven, BE
15. Samal P, Vundavilli PR, Meher A, Mahapatra MM (2020) Recent progress in aluminum metal matrix composites: a review on processing, mechanical and wear properties. J Manuf Process 59:131–152. https://doi.org/10.1016/j.jmapro.2020.09.010
16. Nicholls CJ, Boswell B, Davies IJ et al (2017) Review of machining metal matrix composites. Int J Adv Manuf Technol 90:2429–2441. https://doi.org/10.1007/s00170-016-9558-4
17. Niu Z, Cheng K (2019) An experimental investigation on surface generation in ultraprecision machining of particle reinforced metal matrix composites. Int J Adv Manuf Technol 105:4499–4507. https://doi.org/10.1007/s00170-018-03256-y
18. Sharma DK, Mahant D, Upadhyay G (2020) Manufacturing of metal matrix composites: a state of review. Materials Today: Proceedings, 26. Part 2:506–519. https://doi.org/10.1016/j.matpr.2019.12.128
19. Essien U, Vaudreuil S (2022) Issues in metal matrix composites fabricated by laser powder bed fusion technique: a review. Adv Eng Mater. https://doi.org/10.1002/adem.202200055
20. ISO/ASTM52900:2021 (2021) Additive manufacturing - general principles — fundamentals and vocabulary. ASTM International
21. Gibson I, Rosen D, Stucker B, Khorasani M (2021) Additive manufacturing technology (3rd edition). Springer, Cham. https://doi.org/10.1007/978-3-030-56127-7
22. Bottini L (2021) Study of selective laser melting process parameters to improve the obtainable roughness of AlSi10Mg parts. Selected Topics in Manufacturing. pp 121–139. Springer, Cham. https://doi.org/10.1007/978-3-030-57729-2_9
23. Nuechterlein J, Iten J (2016) Reactive additive manufacturing. Patent Application Publication No. US2016/0271878A1 Sep.22,2016
24. Sullivan E, Polizzi A, Iten J et al (2022) Microstructural characterization and tensile behavior of reaction synthesis aluminum 6061 metal matrix composites produced via laser beam powder bed fusion and electron beam freeform fabrication. Int J Adv Manuf Technol 121:2197–2218. https://doi.org/10.1007/s00170-022-09443-2
25. Jandaghi MR, Pouraliakbar H, Fallah V, Ghassemali E, Saboori A, Pavese M (2022) Additive manufacturing of nano-oxide decorated AlSi10Mg composites: a comparative study on Gd2O3 and Er2O3 additions. Materials Characterization 192:112206. https://doi.org/10.1016/j.matchar.2022.112206
26. AlMangour B (2019) Additive manufacturing of emerging materials. Springer Nature, Cham, Switzerland.
27. (2018) https://www.elementum3d.com/wp-content/uploads/2021/12/An-inside-look-at-how-AM-commercial-aluminum-alloys-are-made-possible-using-RAM-technology.pdf
28. (2021) https://www.elementum3d.com/wp-content/uploads/2021/11/A2024-RAM10-Data-Sheets-2021-04-02-FINAL.pdf
29. Fereiduni E, Ghasemi A (2020) Elbestawi M (2020) Selective laser melting of aluminum and titanium matrix composites: recent progress and potential applications in the aerospace industry. MDPI Aerospace 7(6):77. https://doi.org/10.3390/aerospace7060077
30. Todd I (2017) No more tears for metal 3D printing. Nature 549:342–343
31. Aboulkhair NT, Simonelli M, Parry L, Ashcroft I, Tuck C, Hague R (2019) 3D printing of aluminium alloys: additive manufacturing of aluminium alloys using selective laser melting. Prog Mater Sci 106:100578

32. Tan Q, Zhang J, Sun Q, Fan Z, Li G, Yin Y, Liu Y, Zhang MX (2020) Inoculation treatment of an additively manufactured 2024 aluminium alloy with titanium nanoparticles. Acta Mater 196:1–16. https://doi.org/10.1016/j.actamat.2020.06.026

33. Rometsch PA, Zhu Y, Wu X, Huang A (2022) Review of high-strength aluminium alloys for additive manufacturing by laser powder bed fusion. Mater Des 219:110779. https://doi.org/10.1016/j.matdes.2022.110779

34. Maconachie T, Leary M, Lozanovski B et al (2019) SLM lattice structures: properties, performance, applications and challenges. Mater Des 183:108137. https://doi.org/10.1016/j.matdes.2019.108137

35. Boschetto A, Bottini L, Veniali F (2017) Roughness modeling of AlSi10Mg parts fabricated by selective laser melting. J Mater Process Technol 241:154–163. https://doi.org/10.1016/j.jmatprotec.2016.11.013

36. Parry LA, Ashcroft IA, Wildman RD (2019) Geometrical effects on residual stress in selective laser melting. Addit Manuf 25:166–175. https://doi.org/10.1016/j.addma.2018.09.026

37. Woodard K, Comstock L, Wamboldt L, Sutherland J (2016) Optimum selection of high performance mirror substrates for diamond finishing. Adv Opt Def Appl UV through LWIR 9822:98220C. https://doi.org/10.1117/12.2231326

38. ASTM E8/E8M-04 (2004) Standard test methods for tensile testing of metallic materials. ASTM International, West Conshohocken

39. Stopyra W, Gruber K, Smolina I, Kurzynowski T, Kuźnicka B (2020) Laser powder bed fusion of AA7075 alloy: influence of process parameters on porosity and hot cracking. Addit Manuf 35:101270. https://doi.org/10.1016/j.addma.2020.101270

40. Gu D (2015) Laser additive manufacturing of high-performance materials. Springer-Verlag, Berlin

41. Atkins C, Brzozowski W, Dobson N et al (2019) Lightweighting design optimisation for additively manufactured mirrors. Proceedings Volume 11116, Astronomical Optics: Design, Manufacture, and Test of Space and Ground Systems II. https://doi.org/10.1117/12.2528105

42. Kim S, Chang S, Pak S et al (2015) Fabrication of electroless nickel plated aluminum freeform mirror for an infrared off-axis telescope. Appl Opt 54(34):10137. https://doi.org/10.1364/AO.54.010137

43. Valente T M, Vukobratovich D A (1989) Comparison of the merits of open-back, symmetric sandwich, and contoured back mirrors aslight-weighted optics. Proceedings Volume 1167, Precision Engineering and Optomechanics. https://doi.org/10.1117/12.962927

44. Hedges AR, Parker RA (1989) Low stress, vacuum - chuck mounting techniques for the diamond machining of thin substrates. Proceedings Volume 0966, Advances in Fabrication and Metrology for Optics and Large Optics. https://doi.org/10.1117/12.948045

45. Vrána R, Koutecký T, Červinek O et al (2022) (2022) Deviations of the SLM produced lattice structures and their influence on mechanical properties. MDPI Materials 15:3144. https://doi.org/10.3390/ma15093144

46. Qi D, Yu H, Liu M et al (2019) Mechanical behaviors of SLM additive manufactured octet-truss and truncated-octahedron lattice structures with uniform and taper beams. Int J Mech Sci 163:105091. https://doi.org/10.1016/j.ijmecsci.2019.105091

47. Xu C, Peng X, Liu J et al (2022) (2022) A high efficiency and precision smoothing polishing method for NiP coating of metal mirror. Micromachines 13:1171. https://doi.org/10.3390/mi13081171